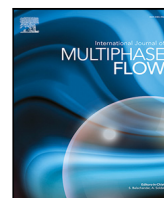




Contents lists available at [ScienceDirect](https://www.sciencedirect.com)

International Journal of Multiphase Flow

journal homepage: www.elsevier.com/locate/ijmulflow



Highlights

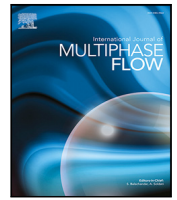
The Corrected Distortion model for Lagrangian spray simulation of transcritical fuel injection

International Journal of Multiphase Flow xxx (xxxx) xxx

Tuan M. Nguyen^{*}, Rainer N. Dahms, Lyle M. Pickett, Fabien Tagliante

- Implementation of a new distorted droplets model for Lagrangian spray simulation of relevant engine condition.
- Model validation in CONVERGE CFD using Engine Combustion Network (ECN) Spray A with detailed liquid phase analysis.
- Examination of the new model impact on the heat and mass transfer using both experiments and 1D adiabatic mixing theory.
- Analysis reveals the need to improve Lagrangian–Eulerian coupling implementation for Large Eddy Simulation (LES).

Graphical abstract and Research highlights will be displayed in online search result lists, the online contents list and the online article, but **will not appear in the article PDF file or print unless it is mentioned in the journal specific style requirement. They are displayed in the proof pdf for review purpose only.**



The Corrected Distortion model for Lagrangian spray simulation of transcritical fuel injection

Tuan M. Nguyen^{a,*}, Rainer N. Dahms^{a,b}, Lyle M. Pickett^a, Fabien Tagliante^a

^a Sandia National Laboratories, Livermore, CA, USA

^b Corporate Strategic Research, ExxonMobil Research and Engineering, Clinton, NJ, USA

ARTICLE INFO

Keywords:

Computational fluid dynamics
Lagrangian diesel spray simulations
Deformed drop
Diffused Back Illumination
Liquid penetration
Internal combustion engine

ABSTRACT

In this work, we present a detailed implementation and validation of the droplet modeling framework proposed by Dahms and Oefelein (2016) into the engine commercial CFD software CONVERGE using the User Defined Function (UDF) interface. The model accounts for the nonlinear deformation and oscillation experienced by liquid spray droplet injected into high pressure and temperature. Lagrangian spray simulations of Engine Combustion Network (ECN) Spray A are performed. Model validation against standard experimental measurements of liquid velocity, vapor mixture fraction is conducted. To perform more rigorous model validation, new experimental measurements based on Diffused Back Illumination (DBI) are introduced. The new measurements are processed for Projected Liquid Volume (PLV), which offers as close as possible one-to-one model validation for liquid penetration while offering new insights into the spray physics. Comparison with a One-D model based on adiabatic mixing theory by Siebers (1999) and Desantes et al. (2007) are also conducted. Through these model validation exercises, it is shown that the new framework improves liquid-phase penetration predictions, following a tendency for enhanced evaporation, compared to the standard approach for both Reynolds Average Navier Stokes (RANS) and Large Eddy Simulation (LES). At the liquid length, maximum mixture fraction values predicted by the new approach are in good agreement those of an adiabatic mixing model. Qualitative analysis of the spray behaviors during the early stage of the injection process reveals that the proposed framework predicts significant increase in droplet evaporation rate with lower drop drag compared to the current standard approach.

1. Introduction

Liquid fuel injection in modern combustion systems is a multi-physics process that involves many different nonlinear phenomena. Two popular classes of approach can be utilized to model such complex systems. In the first approach, the interface between liquid fuel and the ambient gas is resolved using advanced techniques such as volume-of-fluid (VOF) coupled with the level-set method (Tryggvason et al., 2011). Given sufficient resolution, the method can theoretically resolve all associated phenomena such as primary and secondary liquid breakups, droplets collision, coalescence. However, the main drawback of such an approach, as with any high fidelity method, is its expensive computational costs. Furthermore, modeling liquid spray evaporation using VOF calculation is still a challenging task. Another alternative and more computationally affordable method is the Lagrangian–Eulerian framework. In this approach, liquid fuels are modeled as stochastic Lagrangian particles while the gaseous flow

field is solved in the traditional Eulerian formulation. Momentum and heat/mass exchanges processes between the liquid and gas phases is not resolved and have to be modeled. Momentum transfer between liquid droplets and the carrier gas phase is realized through the drop drag coefficient calculation. One of the most popular drop drag coefficient correlation is proposed by Amsden et al. (1989), which derived from characteristics behavior of a perfectly spherical rigid sphere. The heat and mass transfer processes between the liquid and gaseous flow fields are simulated using evaporation models such as those proposed by Ranz and Marshall (1952), Sirignano (1983) and Abramzon and Sirignano (1989). Similar to the drag coefficient studies, these models usually assume liquid drops are perfectly spherical. However, at realistic engine conditions, fuel droplets are usually injected into high pressure and temperature environment that sometime exceeds their critical properties. One example of such condition is the Engine Combustion Network (ECN) Spray A, where cold liquid n-dodecane ($P =$

* Corresponding author.

E-mail addresses: mtnguye@sandia.gov (T.M. Nguyen), rainer.dahms@exxonmobil.com (R.N. Dahms), lpicke@sandia.gov (L.M. Pickett), ftaglia@sandia.gov (F. Tagliante).

<https://doi.org/10.1016/j.ijmultiphaseflow.2021.103927>

Received 14 June 2021; Received in revised form 6 October 2021; Accepted 3 December 2021

1500 bar, $T = 363$ K) is injected in a 900-K and 60-bar environment (Engin Combustion Network, 2021a). Under this condition, the liquid spray experiences intense heat up that leads to rapidly diminishing surface tension. Consequently, liquid fuel droplets experience highly nonlinear deformation and oscillation, as observed during diesel-engine relevant condition injection by Stetsyuk et al. (2015) and Crua et al. (2017).

Therefore, traditional spherical droplet assumptions become questionable under engine relevant conditions. While there are existing models that account for drop non-sphericity effect, their weaknesses can sometime provide inaccurate simulation results. For example, Liu et al. (1993) derived a drag coefficient correlation for highly distorted drops. However, the model assumes distorted drops behave similarly to sharp disks, leading to unrealistically high drop drag coefficient. More recently, to capture the effect of non-sphericity on liquid droplet evaporation, Tonini and Cossali (2013, 2014) derived an analytical model to approximate the heat and mass transfer rate of both oblate and prolate spheroidal drops. However, the model is only valid for fuel drops in stagnant conditions. Using a similar theoretical framework as Tonini and Cossali, Li and Zhang (2014) investigated the evaporation rate of oblate spheroid under a range of Reynolds and Nusselt numbers that are less than 100 and 14, respectively. Zubkov et al. (2017) derived a model for heating and evaporation of non-spherical droplets. The most significant assumption is that the droplet remains spheroidal during evaporation, even though its parameters such as eccentricity are allowed to change with time. Therefore, the models reviewed above, in their current form, cannot yet be applied to realistic engine spray simulations.

Recently, Dahms and Oefelein (2016) proposed a unified framework to account for droplet non-sphericity effects in drop drag and evaporation formulation. The model is valid for both oblate and prolate spheroids in a high-speed spray injection system. First, the transient drop distortion and oscillation are modeled using the Taylor Analogy Breakup (TAB) model. Second, correlations proposed by Feng and Michaelides for perfectly spherical viscous sphere are applied to calculate the drag coefficient, Nusselt, and Sherwood numbers (Feng and Michaelides, 2001a,b). Then, a regression formula, proposed by Richter and Nikrityuk (2012), is applied to correct for droplet distortion effect. Finally, because the Nusselt and Sherwood number is an area-averaged value, an area correction term is applied to account for the difference between a distorted drop and its perfectly spherical counterpart that has the same equivalent radius. The model impact was examined by simulating particle-laden flow in a model gas turbine engine (Sommerfeld et al., 1992). The new approach herein is called the Corrected Distortion (CD) model.

The current paper details our implementation and validation of the Corrected Distortion model into the CONVERGE commercial CFD package. It is, therefore, an extension of the work that was presented by Dahms and Oefelein. However, in contrast to previous work, model results are validated with high quality experimental measurements under relevant engine conditions. The current work also focuses on understanding the CD model's impact on the heat and mass transfer processes between the liquid spray and the ambient gases during injection process. The organization of the paper is as follows. First, particle governing equations and relevant formulas are given to illustrate the difference between the current standard and Corrected Distortion models. The model implementation is then described in detail. Third, description of the numerical solver and validation case is given. Finally, detailed comparisons between simulation results and existing experimental measurements are given.

2. Particle governing equations

In this work, the Corrected Distortion model is implemented into the existing Lagrangian–Eulerian framework within CONVERGE. Detailed implementation and formulation of the overall framework is presented

in Senecal et al. (2007) and Richards et al. (2020a) and will not be presented here for brevity purposes. We will, however, present the particle governing equations to compare and contrast the differences between the standard method and the Corrected Distortion model. Such approach would enable the readers to adapt the CD model into their CFD solver of choice.

The governing equation for particle motions can be written as Richards et al. (2020a)

$$\frac{dv_i}{dt} = \frac{3}{8} \frac{\rho_g}{\rho_d} C_D \frac{U_i}{r} U_i, \quad (1)$$

where v_i is the drop velocity; ρ_g and ρ_d are the gas and liquid density, respectively. U_i is the drop-gas relative velocity and C_D is the drop drag coefficient.

Assuming incompressible liquid, the droplet mass transfer via evaporation can be described as Richards et al. (2020a)

$$\frac{dr_o}{dt} = \frac{\rho_g D}{2\rho_d r_o} B_d S h_d, \quad (2)$$

where D is the mass diffusivity of liquid vapor in ambient gas. r_o is the droplet radius, with $S h_d$ is its Sherwood number. The Spalding transfer number B_d is defined as

$$B_d = \frac{Y_1^* - Y_1}{1 - Y_1^*}, \quad (3)$$

where Y_1^* is the vapor fuel mass fraction at the drop's surface, Y_1 is the local ambient vapor mass fraction. The drop Reynolds number is defined as

$$Re_d = \frac{\rho_g |U_i| d_d}{\mu_g}, \quad (4)$$

with d_d is the drop diameter, μ_g is the ambient gas viscosity

Additionally, Y_1^* is determined from the expression

$$Y_1^* = \frac{M_{C_n H_{2m}}}{M_{C_n H_{2m}} + M_{mix} \left(\frac{\rho_g}{\rho_v} - 1 \right)}, \quad (5)$$

The energy conservation equation is

$$\bar{A}_d \bar{Q}_d = c_l m_d^* \frac{dT_d}{dt} - \frac{dm_d}{dt} H_{vap}, \quad (6)$$

where c_l is the liquid specific heat, T_d is the drop temperature, m_d is the drop mass, and H_{vap} is the latent heat of vaporization evaluated at the drop temperature. The rate of heat conduction to the drop surface (\bar{Q}_d) is given by the Ranz–Marshall correlation (Faeth, 1977)

$$\bar{Q}_d = \frac{Nu_d k_g (T_g - T_d)}{\bar{d}_o}, \quad (7)$$

where k_g is the gas conductivity evaluated at \bar{T} and Nu_d is the Nusselt number.

Furthermore, in the above equations, \bar{A}_d and \bar{d}_o are the average drop area and diameter, respectively; and m_d^* is an intermediate value of the drop mass evaluated at the drop surface. They are given as

$$\bar{A}_d = \frac{\pi(r_o^{*2} + r_o^2)}{2} \quad (8a)$$

$$\bar{d}_o = r_o^* + r_o \quad (8b)$$

$$m_d^* = \frac{4}{3} \rho_l \pi r_o^3. \quad (8c)$$

All the transport properties such as μ_g , k_g are functions of the temperature given by Amsden et al. (1989)

$$\hat{T} = \frac{T_g + 2T_d}{3}, \quad (9)$$

with the mass diffusivity (D) is also a function of \hat{T} , and has the form

$$\rho_g D = 1.293 D_o (\hat{T}/273)^{n_o - 1}, \quad (10)$$

where D_o and n_o are experimentally-determined model constants.

2.1. Current standard model

In Eqs. (11)–(13), the liquid–gas coupling is modeled through the drop drag coefficient (C_D), the Nusselt number (Nu_d), and the Sherwood number (Sh_d). A popular drag coefficient model is Liu et al. (1993)

$$C_{D,sphere} = \begin{cases} \frac{24}{Re_d} \left(1 + \frac{1}{6} Re_d^{2/3}\right), & Re \leq 1000 \\ 0.424, & Re > 1000. \end{cases} \quad (11)$$

The Frossling correlation (Amsden et al., 1989) is a popular approach to model the heat and mass transfer process. The Nusselt number in this approach is given as

$$Nu_d = (2 + 0.6 Re_d^{1/2} Pr_d^{1/3}) \frac{\ln(1 + B_d)}{B_d}, \quad (12)$$

with the Sherwood number as

$$Sh_d = (2 + 0.6 Re_d^{1/2} Sc_d^{1/3}) \frac{\ln(1 + B_d)}{B_d}, \quad (13)$$

where the drop Prandtl number (Pr_d) has the form

$$Pr_d = \frac{\mu_s C_p}{\lambda_s}, \quad (14)$$

where the Schmidt number (Sc_d) of the drop and has the form

$$Sc_d = \frac{\mu_g}{\rho_g D}. \quad (15)$$

C_p is the constant specific heat. λ_s is the drop thermal conductivity and should not be confused with the viscosity ratio λ in Eqs. (17) and (19).

There is currently no unified standard framework to account for drop non-sphericity in both drag and evaporation model. Furthermore, even when non-sphericity of droplet is considered, as in the case of drag coefficient, the correlation is based on unrealistic assumption that highly distorted drop will behave as a sharp disk. This assumption leads to the following correlation (Liu et al., 1993)

$$C_D = C_{D,sph}(1 + 2.632y), \quad (16)$$

where y is the non-dimensional droplet distortion factor, as determined by the TAB model (O'Rourke and Amsden, 1987). Motivated by the limitation of the current approach, the following section presents a new unified framework, as originally proposed by Dahms and Oefelein (2016), that accounts for both deformation effects and variable droplet viscosity in the model formulations as opposed to simple solid sphere correlations.

2.2. Corrected distortion model

Fig. 1 shows the flow field around different spheroids characterized by different distortion parameter (y) values. The ambient flow is from left to right. When y is negative, a drop is classified as a prolate spheroid, where its major axis is parallel to the flow direction, resulting in reduced drag compared to a perfectly spherical drop with the same equivalent radius. When y is positive, drop is classified as an oblate spheroid, with its major axis being perpendicular to the flow direction, resulting in increased drag compared to perfectly spherical drop with the same equivalent radius.

The Corrected Distortion model is formulated to accurately capture the correct physics illustrated in Fig. 1. To the best of the authors' knowledge, this is the first time the model is applied for simulations of trans-critical fuel injection process under relevant engine condition.

2.2.1. Model for viscous spherical drops

The drag coefficient for a viscous spherical droplet is Feng and Michaelides (2001a)

$$C_{D,sph} = \begin{cases} \frac{2-\lambda}{2} C_{D,b} + \frac{4\lambda}{6+\lambda} C_{D,2}, & (0 \leq \lambda \leq 2; 5 < Re < 1000), \\ \frac{4}{2+\lambda} C_{D,2} + \frac{\lambda-2}{\lambda+2} C_{D,s,sph}, & (2 \leq \lambda \leq \infty; 5 < Re < 1000). \end{cases} \quad (17)$$

where λ is the viscosity ratio between the liquid and gas ($\lambda = \mu_l/\mu_g$). $C_{D,b}$, $C_{D,2}$, $C_{D,s,sph}$ are the drag coefficients of bubble, $\lambda = 2$ and solid sphere. They are given as

$$C_{D,b} = \frac{48}{Re_d} \left(1 + \frac{2.21}{\sqrt{Re_d}} - \frac{2.14}{Re}\right) \quad (18a)$$

$$C_{D,2} = 17 Re^{-2/3} \quad (18b)$$

$$C_{D,s,sph} = \frac{24}{Re_d} \left(1 + \frac{1}{6} Re_d^{2/3}\right). \quad (18c)$$

Note that Eqs. (18c) and (11) have the same form, which means the current standard approach only considers liquid droplets as solid spheres with infinite viscosity. The Corrected Distortion model accounts for finite viscosity effect of the liquid droplets, which is more physically sound compared to the standard approach.

The Sherwood formulation for viscous spherical droplets is defined as Feng and Michaelides (2001b)

$$Sh_{vis,sph} = \begin{cases} \frac{2-\lambda}{2} Sh_b + \frac{4\lambda}{6+\lambda} Sh_2, & (0 \leq \lambda \leq 2; 5 < Re < 1000), \\ \frac{4}{2+\lambda} Sh_2 + \frac{\lambda-2}{\lambda+2} Sh_{s,sph}, & (2 \leq \lambda \leq \infty; 5 < Re < 1000), \end{cases} \quad (19)$$

where the Sherwood correlations for the bubble, intermediate viscosity, and solid spheres are given as

$$Sh_b = 0.651 Pe_{Sh}^{1/2} \left(1.032 + \frac{0.61 Re_d}{Re_d + 21}\right) + \left(1.60 - \frac{0.61 Re_d}{Re_d + 21}\right), \quad (20a)$$

$$Sh_2 = 0.64 Pe_{Sh}^{0.43} \left(1 + 0.233 Re_d^{0.287}\right) + 1.41 - 0.15 Re_d^{0.287}, \quad (20b)$$

$$Sh_{s,sph} = 0.852 Pe_{Sh}^{1/3} \left(1.0 + 0.233 Re_d^{0.287}\right) + 1.3 - 0.182 Re_d^{0.355}, \quad (20c)$$

where the Peclet number for mass transfer is

$$Pe_{Sh} = Sc_d Re_d. \quad (21)$$

The Nusselt number, which accounts for the heat transfer process, has the same functional form as ones presented in Eqs. (19)–(20). However, the Peclet number now is calculated based on the Prandtl number

$$Pe_{Nu} = Pr_d Re_d. \quad (22)$$

2.2.2. Correlation for viscous distorted drops

Further correlation between spherical and distorted drops is needed to capture the correct physical behavior of distorted drops. Richter and Nikrityuk (2012) derived a regression model that predicts 99.8 percent of the variance of the drag coefficient, which has the form

$$\frac{C_D}{C_{D,vis,sph}} = \frac{0.21 + \frac{20}{Re_d} \left(\frac{l}{d_d}\right)^{0.58} + \frac{6.9}{\sqrt{Re_d}} \left(\frac{l}{d_d}\right)^{-1.4}}{0.21 + \frac{20}{Re_d} + \frac{6.9}{\sqrt{Re_d}}}, \quad (23)$$

where l is the drop's spanwise length and has the form

$$l = 2r_d(1 - C_b y), \quad (24)$$

where C_b is one of the TAB modeling constant and has a value of 0.5 (O'Rourke and Amsden, 1987).

As the drops are distorted, their surface areas increase compared to undistorted ones with the same equivalent radius. Richter and Nikrityuk (2012) have identified the sphericity ϕ and the cross-wise sphericity ϕ_{\perp} as the main geometric parameters that account for the variation

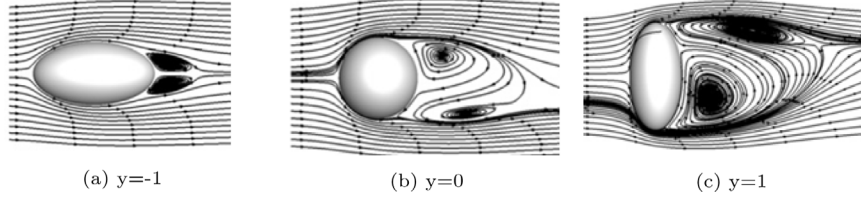


Fig. 1. Distorted drop classified by the distortion factor for (a) prolate spheroid, (b) spherical drops and (c) oblate spheroid.
Source: Reprinted from Richter and Nikrityuk (2012).

of Sherwood numbers due to drop distortion. Similar to Eq. (23), the correlation of Sherwood number has the form

$$\frac{Sh}{Sh_{vis,sph}} = \frac{1.76 + 0.55\phi Sc_d^{1/3} \sqrt{Re_d} \phi_{\perp}^{0.075} + 0.014 Sc_d^{1/3} Re_d^{2/3} \left(\frac{\phi}{\phi_{\perp}}\right)^{7.2}}{1.76 + 0.55 Sc_d^{1/3} \sqrt{Re_d} + 0.014 Sc_d^{1/3} Re_d^{2/3}}, \quad (25)$$

where the sphericity is defined as

$$\phi = \frac{4\pi r_d^2}{Srfc_d}, \quad (26)$$

and the cross-wise sphericity is

$$\phi_{\perp} = \left(\frac{r_d}{H}\right)^2. \quad (27)$$

In the above equations, $Srfc_d$ is the surface area and H is the half length of the crosswise axis with respect to flow direction of the deformed drop. The volume of these spheroids are

$$V = \frac{4}{3}\pi r_d^3 = \frac{4}{3}\pi LH^2, \quad (28)$$

with H as

$$H = \sqrt{\frac{r_d^3}{L}} = \frac{r_d}{\sqrt{1 - C_b y}}, \quad (29)$$

where $L = r_d(1 - C_b y)$. The surface area is then computed as

$$Srfc_p = \begin{cases} 2\pi H^2 \left(1 + \frac{1-e^2}{e} \tanh^{-1}(e)\right), & y \geq 0, \\ 2\pi H^2 \left(1 + \frac{1}{He} \sin^{-1}(e)\right), & y < 0, \end{cases} \quad (30)$$

with the eccentricity e defined as

$$e = \sqrt{1 - \left(\frac{\min(H, L)}{\max(H, L)}\right)^2}, \quad (31)$$

The correlation for the Sherwood number has the same form as in Eq. (25) but with the Prandtl number being replaced by the Schmidt number. However, unlike the drag coefficient, which implicitly includes the surface area variation, Eq. (25) and its corresponding Nusselt number formulation only compute the averaged-surface-area value. Therefore, the final correction needs to take into account the increased surface area of the distorted drop, which means

$$\frac{dm_d}{dt} \Big|_{vis,n sph} = \frac{dm_d}{dt} \Big|_{vis,sph} \frac{Sh}{Sh_{s,sph}} \frac{Srfc_d}{\pi d_d^2}, \quad (32)$$

where the term $\frac{dm_d}{dt} \Big|_{vis,sph}$ is proportional to the left hand side of Eq. (2)

3. Numerical implementation

The previously described standard approach refers to a popular framework implemented in many different codes (Som et al., 2012; Desantes et al., 2019). This approach combines the drag coefficient calculated by correlation from Liu et al. (1993) and the Frossling correlation for droplet evaporation (Amsden et al., 1989). The Corrected

Distortion framework uses the combined approach for both drag and evaporation of viscous spheroid described in the previous section. For further clarity, Table 1 summarizes the implementation procedure for both the standard and Corrected Distortion models.

For validation, simulations of ECN Spray A (Engine Combustion Network, 2021a) are carried out using both the standard as well as the proposed Corrected Distortion models. The standard model has been used for many simulation using CONVERGE. It is widely accepted that making adjustments to various parameters such as spray cone angle, initial turbulence intensity, cell density, etc., will have some influence on results and potentially confound the influence of the spray model itself. Our approach is to fix model input parameters based upon available experimental measurements such as initial conditions, spray cone angle, as well as other accepted inputs for the standard model from previous studies. For example, mesh sizes used in this study are selected based on previous grid convergence studies for RANS (Senecal et al., 2012) and LES (Senecal et al., 2014). In addition, we introduce a more rigorous comparison of measured liquid penetration to simulation results. In the past, either the experiment did not have a precise definition, or the simulations were not processed using the same metric, leading to incomplete conclusions. With commitment to use standard inputs in both models as well as more detailed and quantitative comparison to experiment, our objective is to clearly reveal the effect of the new Corrected Distortion model. Using such approach, we seek to clarify the influence of specific model terms through control of other experimental/modeling parameters.

A total of eight simulations have been performed using CONVERGE 3.0 CFD solver (Richards et al., 2020b). Two RANS simulations, one with the standard models provided in CONVERGE and the other with the Corrected Distortion model. Then, six LES simulations, with 3 realizations for each approach are performed. Table 2 shows the spray modeling parameters used in both LES and RANS simulations. The Rate of Injection (ROI) and injected droplet diameter are modeled by injector characteristics described in Engine Combustion Network (2021b). Turbulence is modeled using either standard $k - \epsilon$ for RANS or Dynamic Structure for LES. The only other difference between the LES and RANS simulations is the mesh resolution. For both turbulence modeling approaches, fixed cell embedding and Adaptive Mesh Refinement (AMR) are used to efficiently resolve the spray structure. The fixed embedding zone is a 7 mm length cone centered on the injector, with a first radius of 1 mm at the nozzle tip and a second radius of 2 mm downstream. Table 3 shows the different base grid resolutions and AMR strategies used for RANS or LES as well as some computational details.

4. Results and discussions

While Spray A has extensive experimental data for model validation, one must recognize the difference in the initial/boundary conditions of these experimental campaigns. For example, these experiments have been performed at different institutions or with different serial numbers of the same nominal injector. Therefore, in the following section, we will list the injector serial number used in different experiments in the figure captions, to emphasize the challenges of a true one-to-one experimental and modeling comparison.

Table 1

Comparison between implementation procedure between the standard and Corrected Distortion models. The Nusselt number has the same formulation as the Sherwood number, but are functions of Prandtl number instead of Schmidt number.

	Momentum transfer (C_D)		Mass transfer, (Sh_d)		Heat transfer, (Nu_d)	
	Std	Corr. distortion	Std	Corr. distortion	Std	Corr. distortion
(1.) Spherical drop	Eq. (11)	Eq. (17)	Eq. (13)	Eq. (19)	Eq. (12)	Eq. (19)
(2.) Shape correction	Eq. (16)	Eq. (23)	N/A	Eq. (25)	N/A	Eq. (25)
(3.) Area correction	Implicit	Implicit	N/A	Eq. (32)	N/A	Eq. (32)

Table 2

Spray modeling parameters used for both LES and RANS simulations. The abbreviation CD corresponds to Corrected Distortion.

Spray modeling parameters	
Droplet type	Lagrangian parcel
Breakup model	MOD-KH-RT (Beale and Reitz, 1999; Senecal et al., 2007)
Vaporization	Frossling (Amsden et al., 1987) or CD-Frossling coupled model
Droplet collision	No time counter (NTC) (Schmidt and Rutland, 2000)
Droplet drag	Dynamic sphere (Liu et al., 1993) or CD model
Droplet dispersion	O'Rourke (Amsden et al., 1987)
Droplet diameter	89 μm
Nozzle diameter	90 μm
Cone angle	20
Discharge coefficient (Cd)	0.83
Velocity coefficient (CV)	Dynamic
Injection duration	1.54 ms
Total mass injected (mg)	3.46

Table 3

Mesh characteristics for LES and RANS simulations.

	RANS	LES
Base grid [mm]	8	8
Fix embedding level	6	7
AMR embedding level	6	7
AMR criteria	Velocity	Velocity and temperature
Minimum grid resolution [mm]	0.125	0.0625
Maximum cell count	1 million	10 million
Initial subgrid tke (Engine Combustion Network, 2021c; Sphicas et al., 2017)	0.0005	0.0005

4.1. Overall vapor phase validation

Fig. 2 presents the vapor penetration for all cases. The vapor penetration is defined as the farthest distance where the mixture fraction is 0.001 (Pickett et al., 2011). The LES results are in excellent agreement with experimental measurement. The RANS results match the experimental measurement very well during the early stage of the injection process ($t \leq 0.4$ ms), but under-predict during the later period. It is noted that the vapor penetration prediction can be improved by applying Pope's round jet correction for the RANS simulations (Desantes et al., 2019).

Unless otherwise noted in the figure caption, for the remaining figures in this work where either radial or axial profiles are shown, the following rules are applied:

1. All profiles are time-averaged during the quasi-steady period from 0.9–1.5 ms
2. For each model combination, all LES results are interpolated onto a uniform grid, then ensemble- (realization-) averaged across all three simulations.

Figs. 3 shows the comparison of the mixture fraction profile in the transverse direction to the spray axis at $x=25$ mm for both simulations and experimental measurements (Pickett et al., 2011; Meijer et al., 2012). Because of the high degree of uncertainty in the region upstream of 30 mm in the velocity measurements (Malbec et al., 2020), Fig. 4

shows the transverse profile comparison of the velocity at 30 mm downstream of the injector.

Fig. 5 shows axial velocity and mixture fraction profiles at the injector axis compared to experimental data for all simulations. Because the quasi-steady requirement of time averaging, only data upstream of 40 mm is shown in these figures since the vapor jet passes 40 mm right before 0.9 ms (cf. Fig. 2).

Regardless of the model combination, the simulations shows reasonable agreement to the available experimental data for vapor phase penetration, velocity and mixture fraction, similar to past work using CONVERGE such as Senecal et al. (2014). Having established this baseline, we can focus on spray modeling differences introduced with the new Corrected Distortion model. Both steady-state and early transient spray behavior will be analyzed, mainly focus on the liquid spray characteristics. In the next section, we will first compare the Projected Liquid Volume results between simulations and experiments. Emphasis will be placed on how to post-process the data for PLV to define the liquid length and to elucidate additional insights into how the liquid spray is behaving. Then, comparison between the CFD and a 1D evaporative spray model by Desantes et al. (2007) is presented in the context of heat and mass transfer. Finally, qualitative examination of physical spray characteristics during the early stage of the injection process is presented.

4.2. Quasi-steady liquid spray behavior

4.2.1. Projected liquid volume and liquid penetration

While liquid-phase penetration is one of the most popular metrics used in the literature for model validation, a thorough examination shows that there are many uncertainties associated with such a basic comparison. The first source of uncertainty is the experimental technique used to measure liquid penetration. Historically, Mie-scattering has been the chosen approach (Siebers, 1998; Zhang et al., 1997). However, as detailed by Pickett et al. (2015), a light scattering technique is sensitive to the orientation of the illumination source. Furthermore, the complex relationship between the local liquid volume fraction and the light scatter/extinction intensity creates additional uncertainty about the accuracy of the measured liquid-phase penetration. Rather than relying on arbitrary Mie-scattering setups and definitions, light extinction diagnostics are more quantitative because of the built in reference intensity (Manin et al., 2012; Pickett et al., 2015). However, extinction diagnostics at the diesel spray conditions of interest suffer from intense beam-steering effects (on the order of 100 mrad Musculus and Pickett, 2005) due to refractive index gradients, which must be considered to distinguish particles from beam steering. Westlye et al. (2017) recently demonstrated that a Diffused Back Illumination (DBI) setup with an engineered diffuser for adequate radiance may accommodate severe beam steering in an imaging setup, thus providing accurate extinction along the cross-stream direction.

For better comparison to simulations, the measured extinction may be converted to Projected Liquid Volume (PLV) by applying Mie extinction theory and optical parameters such as collection angle and wavelength (Pickett et al., 2015). Ultimately, these extinction-based diagnostics can offer improved one-to-one comparisons between CFD and optical diagnostics. The liquid spray experimental data from a DBI

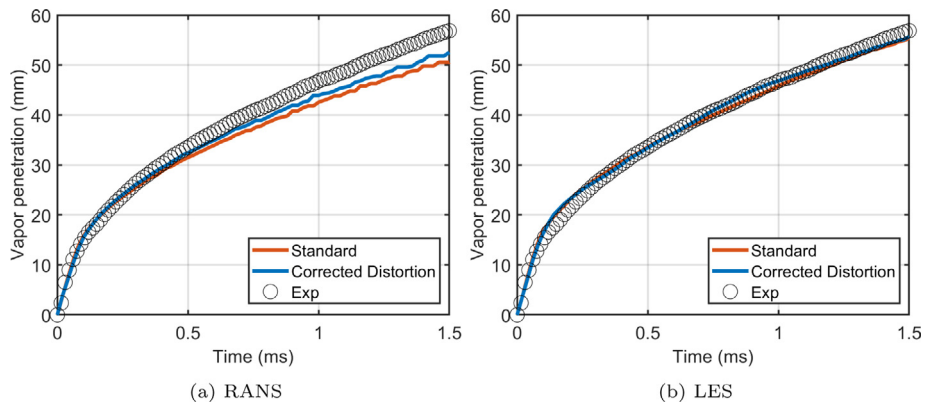


Fig. 2. Comparison of vapor lengths. Experimental data for injector #210677 is shown (Pickett et al., 2011).

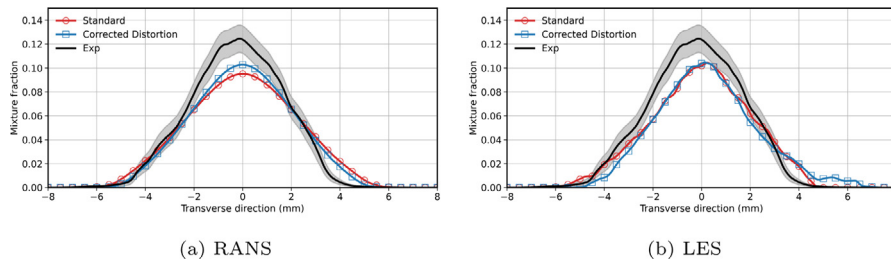


Fig. 3. Comparison of transverse gaseous mixture fraction profiles at 25 mm downstream of the injector. Injector #210677 was used for the experiments (Pickett et al., 2011).

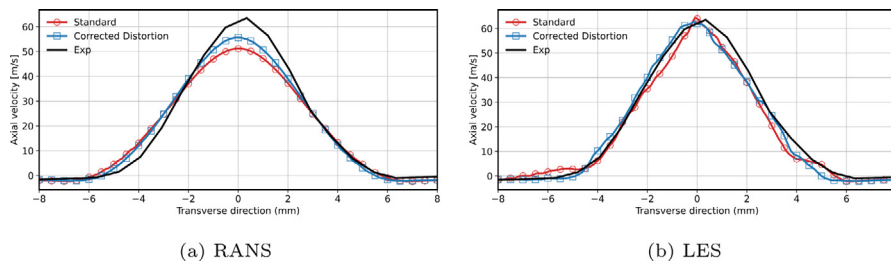


Fig. 4. Comparison of the transverse gaseous velocity profile at 30 mm downstream of the injector. Injector #210678 was used for the experiments (Meijer et al., 2012).

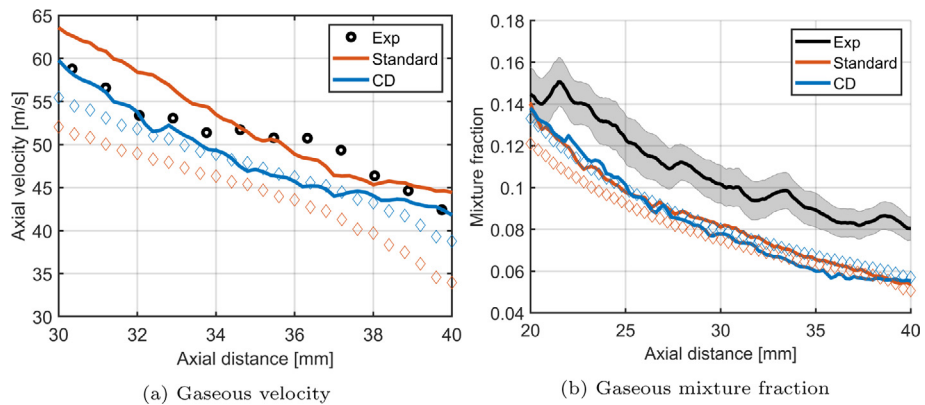


Fig. 5. Comparison of axial profiles for gaseous velocity and mixture fraction for both RANS and LES. Solid lines denote LES realization-averaged results while symbols denote RANS data. Injector #210678 was used for velocity measurements (Meijer et al., 2012), and injector #210677 was used for the mixing measurements (Pickett et al., 2011).

setup is published here for the first time using Spray A nozzle 210370. Furthermore, use of PLV for more rigorous comparison to CFD predictions in gasoline sprays has been demonstrated recently (Paredi et al., 2020) and extended in this work for vaporizing diesel-like condition. Therefore, PLV based method is the ECN recommended standard. The readers are referred to Westlye et al. (2017) for a complete description

of the experimental setup, and to Engine Combustion Network (2021d) for time-resolved two-dimensional image maps and maximum liquid penetration at defined thresholds presented in this work.

One well-known issue with Mie extinction is that there remains a strong dependency upon droplet size, requiring as assessment of droplet size experimentally. While the droplet size in the vaporizing spray at

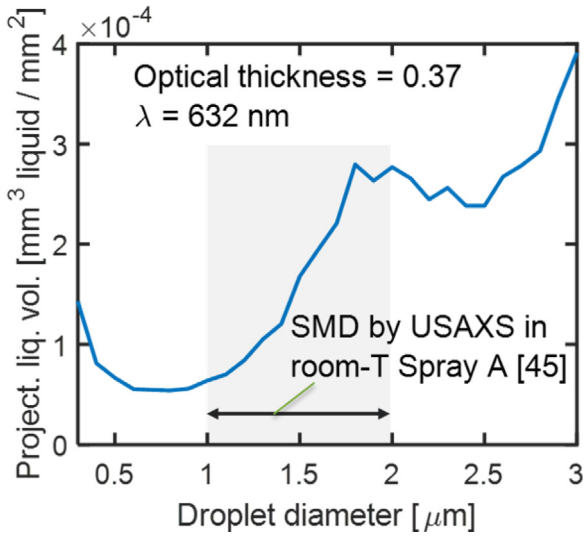


Fig. 6. Projected liquid volume calculated with different droplet sizes for constant optical thickness.

the liquid length position is unknown, droplet sizing measurements have been performed by Kastengren et al. using ultra-small angle x-Ray scattering (SAXS) (Kastengren et al., 2017) in room-temperature Spray A cases at positions that correspond to the liquid length. They found that the spray quickly reaches terminal Sauter mean diameter (SMD) of 1–2 μm within 2 mm downstream of the nozzle exit. The threshold for PLV to define the liquid penetration is based on an optical thickness value of 0.37. This value corresponds to the historical side-imaging Mie-scattering intensity thresholds used to define liquid penetration in a large dataset provided by Siebers (Siebers, 1998). For a constant optical thickness value, Pickett et al. (2015) computed the path-length-averaged LVF as a function of different droplet sizes. With an assumed path-length of 1.4 mm based on spray thickness measurement at the liquid length (Pickett et al., 2015), Fig. 6 shows how the PLV varies as a function of droplet diameter when the optical thickness is held constant at this target value of 0.37.

The oscillation in extinction response with droplet diameter is a complex response in Mie theory as the droplet diameter approaches the 632-nm wavelength of the light. Utilizing the SAXS measurements for SMD produces an expectation that the threshold PLV should be defined somewhere between $1\text{e-}4$ to $3\text{e-}4 \text{ mm}^3\text{liquid}/\text{mm}^2$. However, uncertainties are not specifically published for the SAXS measurements, so it is unknown if the band could be even larger. In addition, as the SAXS measurements apply to room temperature, non vaporizing sprays (ambient density was fixed at the target Spray A condition) (Kastengren et al., 2017), there is a strong expectation that vaporization will change the droplet size distribution at the defined liquid length region. While droplet size would be expected to get smaller at the point of final vaporization, larger droplets may also be more prone to survive. We will specifically investigate this phenomenon by examining the predicted SMD evolution as the spray approaches the liquid length for the different simulations included in this work. While uncertainties are significant, as stated above, we define the liquid penetration as furthest axial distance where PLV is $2.0\text{e-}4 \text{ mm}^3\text{liquid}/\text{mm}^2$. This value specifically corresponds to a droplet diameter of 1.6 μm , as seen from Fig. 6. We reiterate that the PLV definition offers consistency between experiment and simulations, and is superior to an upstream-mass-based definition, even though this definition may have been traditionally applied for liquid length.

The second source of uncertainty is the liquid penetration definition in CFD. Fig. 7 shows the liquid-phase penetration length compared to experimental measurements for both LES and RANS simulations.

The experimental liquid penetration is defined as the farthest axial distance where PLV is less than $2.0\text{e-}4 \text{ mm}^3\text{liquid}/\text{mm}^2$. Traditionally, CFD researchers have employed a different definition. Liquid penetration results in the past have been defined as the furthest distance that contains a certain percentage of upstream liquid mass (Senecal et al., 2014). Specifically, the solid and dotted line in Fig. 7 represent results obtained by using the 97% and 99% of the liquid mass criteria, respectively. Fig. 7 shows that the interpretation of how well the simulations agree with experimental measurements depends arbitrarily on the criteria one chose to define liquid penetration. Furthermore, the criteria chosen here for validation (percentage of upstream mass) does not hold any physical correlation associated with the experimental extinction measurement processed for PLV. Note that other metrics for comparison such as Liquid Volume Fraction rely on 3D experimental data that does not exist, or there is a requirement for a secondary element such as a defined path length that may be arbitrary in definition experimentally (Pickett et al., 2015) or require additional post-processing over that length in the simulation results to remove local grid size dependencies. Extinction profiles that include simulation droplet size dependencies are also possible (Magnotti and Genzale, 2015) but would make it impossible to compare to only liquid volume along the integrated path.

The remainder of this section now focuses comparing the PLV and consequently the liquid penetration for both simulations and experimental measurements. It is defined as

$$PLV(x, z) = \int_{-y_{\infty}}^{y_{\infty}} LVF(x, y, z) dy, \quad (33)$$

where LVF is the Liquid Volume Fraction. In CFD, LVF is the percentage of liquid fuel volume contained within a single Eulerian (gas) cell volume and y denotes any cross-stream direction. The result PLV maps for both CFD and experiments are functions of both the axial direction (x) and the other transverse direction (z).

Fig. 8 compares an instantaneous snapshot of the PLV results obtained from CFD and experimental measurement. The solid blue iso-contour marks the liquid boundary based on the PLV threshold of $2\text{e-}4 \text{ mm}^3\text{liquid}/\text{mm}^2$. The furthest axial distance of this iso-contour denotes the liquid penetration length. Broken vertical lines mark the liquid penetration location obtained from different methods. In Fig. 8(a), the PLV is obtained by integrating LVF over the y direction. Because of the fixed embedding and AMR employed in the computation, the integration is first performed by integrating over all cells with unique z and x coordinate. With this approach, we avoid the expensive 3D interpolation step. Therefore, Fig. 8(a) represents the truly raw projected characteristic of the liquid spray. One can immediately observed the stochastic behavior of the liquid spray in LES simulations, where small liquid droplets can be randomly separated from the main liquid core and travel much further downstream. In this instance, a small cluster of liquid volume can even be sufficiently large that their presence is visible in the PLV map.

In this sense, the spatial resolution of the experiment compared to the simulation must be considered. For example, the experimental data has an imaging pixel resolution of 0.1 mm, and a requirement to spatially resolve features would have an even larger sample size (e.g. 0.2 mm for a Nyquist criteria). To make comparisons more straightforward, the simulation resolution for PLV can be enlarged to correspond to the experimental resolution. A coarsening operation is especially important for LES simulations where the smallest cell width (62.5 μm) is much smaller than experimental resolution. The raw 2D PLV results are therefore mapped/down-sampled onto a uniform coarser mesh. In this case, the down-sample mesh has the same resolution of the experimental data, or 0.1 mm. While the down-sampled PLV map results in shorter liquid length compared to the raw method, the liquid length position remains defined by a small liquid island, even in a line-of-site (projected) integration, detached from the main spray. Considering the significance of such fluctuations, particularly for

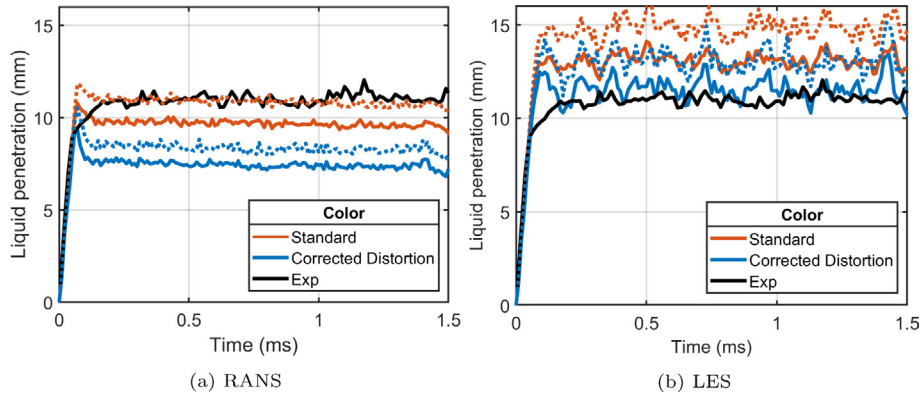


Fig. 7. Comparison of liquid lengths between RANS and LES. Solid lines denote liquid length defined by the furthest axial distance that contains 97% of the liquid mass while the dotted lines correspond to the 99% liquid mass definition. Experimental data, processed using $0.2e-3 \text{ mm}^3 \text{ liquid}/\text{mm}^2$ PLV threshold, for injector #210370 is shown.

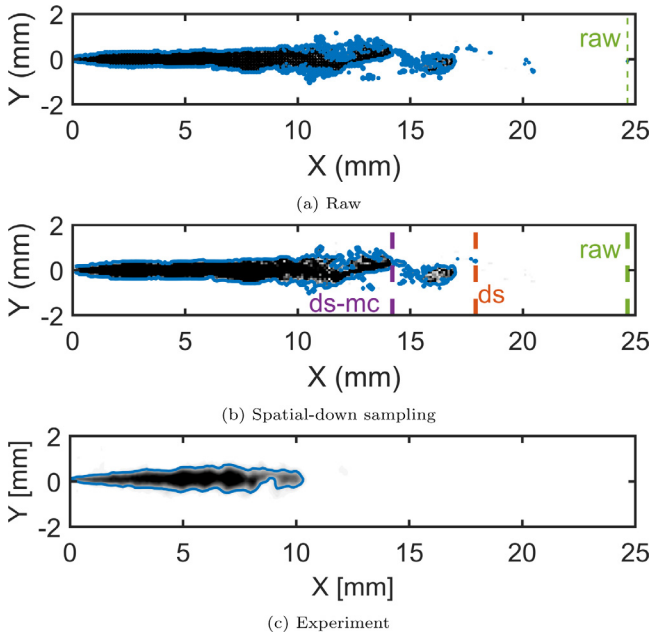


Fig. 8. Instantaneous PLV map at $t = 0.98$ ASOI for a single LES with standard approach and experimental realization. DS is the abbreviation for spatial down sampling. MC is the abbreviation for the main core.

LES compared to the temporally resolved and high-speed experimental extinction imaging, the liquid penetration was also evaluated/defined as the furthest distance where there is no break in connected PLV, or a connected main core region. The liquid penetration with both downsampling (DS) and connected main core (MC) yields a shorter liquid length compared to other definitions.

Fig. 8 illustrates that care must be taken to when post-processing the simulations. In the raw projection data, the effect of mismatched resolution can locate the liquid penetration at an “island” of downstream liquid. With either interpolating the raw 3D field before projection, or the 2D projected field of the raw 3D data such as one employed in the DS method, we can further reduce the mismatching effect. Using the MC definition results in shorter liquid penetration while also offering a consistent basis for comparison. However, one should also note that this is not the experimental definition, but rather an effort to apply different filtering techniques that enable us to establish a physically consistent method for defining liquid penetration in the simulations. To that end, Fig. 9 presents an overall comparison between different liquid penetration profiles from the proposed methods. Only results from the

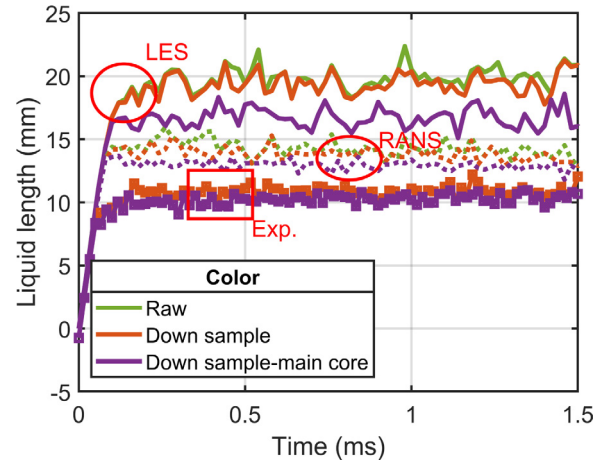


Fig. 9. Transient liquid penetration profile for the standard modeling approach. Line colors are the same as shown for the procedures in Fig. 8.

standard approach are presented here. Solid lines are the LES ensemble-averaged results from three different realizations. Broken lines are the RANS results. Solid lines with symbols are the experimental measurements. There is no significant difference between the raw and down sample method. Resorting to a “main-core” definition shortens liquid penetration by 3 mm in the LES, 1 mm in the RANS, and 0.5 mm in the experimental results. Regardless of the filtering techniques, the standard model predicts much longer liquid penetration compared to the experimental measurements. It should be restated that while the PLV-based definition results in over-prediction in liquid penetration, the simulations here are considered “well-validated” if the traditional mass base definition is used, as shown in Fig. 7, but this is not consistent with the experiment. To the best of the authors’ knowledge, there has not been any PLV-based analysis for liquid penetration under Spray A conditions in existing literature.

Fig. 10 shows the liquid penetration comparison between all simulations results and experimental data. For consistency and clarity purposes, only the down sample with main core method is shown here. LES results are ensemble-averaged across three different realizations. Compared to the penetration curves shown in Fig. 7, one can have more confidence that the results are as close as possible to one-to-one comparison.

While the liquid penetration results in Fig. 10 suggest that RANS simulations are in better agreement with experimental measurements, one should note that RANS simulations at 25 mm are producing wider vapor mixture fraction profile with lower value at the centerline, as shown in Fig. 3. Therefore, we need to further analyze the liquid

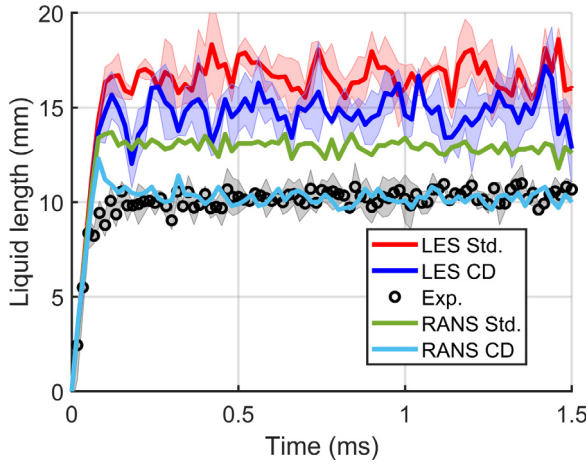


Fig. 10. Comparison of the transient liquid penetration profiles between different turbulence and spray models. All curves are obtained using the down sampled Main Core (MC) method. Shaded regions indicate 1 standard deviation.

spray behavior, both in the axial and transverse directions, for a more complete picture. Fig. 11 shows the PLV transverse profile comparison during the steady-state period in the region upstream of the liquid length. Because of the high optical thickness concerns, which can render the measurement inaccurate where optical thickness > 2 , experimental PLV value larger than $7.5e-4 \text{ mm}^3 liq/mm^2$ are not shown. Consistent with the axial liquid length, we also define the liquid spray width as the distance across the spray where $PLV = 2e-4 \text{ mm}^3 liq/mm^2$ as illustrated by the intersection between all the curves and the broken horizontal line in Fig. 11. At an axial distance of 10 mm where the experimental data are not affected by optical thickness concerns, the RANS with CD model predicts more reasonable PLV magnitude and the other cases predict much higher magnitude that leads to longer liquid penetration prediction. Unfortunately, it under-predicts the liquid spray width at both 8 and 10 mm. The remaining 3 simulations are in reasonable agreement with the measurements at 8 mm.

Fig. 12(a) shows the PLV axial profile at the center of the spray. While the same conclusion can be drawn from Fig. 11 with regards to the magnitude differences, the PLV slopes in all RANS cases are much steeper compared their LES counterparts. In fact, from the experimental measurement, we define the region downstream of 9 mm, where the PLV is less than $7.1e-4 \text{ mm}^3 liq/mm^2$, as the spray tip region. Shifting the spray tip of all simulations results upstream, based on the same definition, serendipitously indicate that LES results are in better agreement with the measurement, as shown in Fig. 12(b). At least the shape of the decline in PLV in the liquid length region looks more appropriate for LES compared to RANS simulations. We will explore this shape in more detail next.

As previously mentioned at the beginning of this section, there is an uncertainty associated with the PLV experimental measurements where a constant droplet size of $1.6 \mu\text{m}$ is assumed based on SAXS measurement under cold, non-vaporizing conditions. To examine the validity of this assumption, especially at the liquid length region, the following section presents a predicted droplet size analysis for all simulation results, particularly in the liquid-length region. For all Eulerian cells that contain spray particles, the SMD is computed based on the formula.

$$SMD = 6 \frac{V_d}{A_d} \quad (34)$$

Where V_d and A_d are the total volume and surface area of all droplets found within an Eulerian cell, respectively. To consolidate statistics, we also apply averaging along the radial direction for a given axial position. The radial-averaged SMD may be analyzed for different

simulations by plotting results during the quasi-steady period versus the axial PLV profiles shown in Fig. 12(a) to examine any potential PLV correlations with droplet size. The downstream region ($> 5 \text{ mm}$) approaching the liquid-length region is featured in Fig. 13. The symbols denote the raw behavior, and the solid lines represent a 2nd order polynomial curve fit. The following discussion examines the validity and accuracy of droplet size correlation and its applicability toward experimental diagnostics.

While LVF obviously decreases in a vaporizing flow, it is not a given that SMD would decrease since small droplets in a distribution tends to vaporize quicker. As observed from Fig. 13(a), the CFD predictions show a monotonic decreasing behavior for PLV and SMD when approaching the liquid length. The simulations show a decline in SMD from $3.0 \mu\text{m}$ to final vaporization value of $0 \mu\text{m}$, but with dependencies upon the spray or turbulence model. The Corrected Distortion model shows smaller droplet sizes for the same PLV, particularly, for the LES simulations. While the experimental assumption of $1.6 \mu\text{m}$ falls within the range of predicted SMD, a change in SMD has implications towards interpretation of the experimental PLV, as discussed in Fig. 6. As seen from Fig. 13(b), the simulations predict droplet sizes less than $0.4 \mu\text{m}$ at the ECN-defined PLV threshold for the liquid length regardless of the modeling approach. For a given turbulence model, the standard approach tends to produce larger droplets compared to its CD model counterpart due to its inability to completely evaporate smaller droplets. Therefore, the standard approach tends to produce small clusters of droplets that persist well after the defined liquid length region as corroborated by Figs. 8–12(a).

Because droplet sizes vary in the simulation results compared to the experimental assumed value, it is interesting to consider how the experimental PLV would respond to different or evolving droplet sizes, as shown in Fig. 14. Recall that the baseline assumption of $1.6 \mu\text{m}$ is based on room-temperature SAXS measurements (Kastengen et al., 2017). Therefore, regardless of the turbulence model, the standard approach over-predicts droplet sizes with SMD values larger than $1.5 \mu\text{m}$ at 5 mm for evaporating conditions. In contrast, the CD model predicts droplet sizes that are much smaller than the SAXS measurement. If the trend of decreasing SMD while approaching the liquid length is real, there is a potential for the correlations to address uncertainties in the experiment. We can therefore consider expected changes in the PLV profile with axial distance. A larger droplet size in upstream regions (e.g., from $1.6 \mu\text{m}$ to $3.0 \mu\text{m}$) increases the PLV. In fact, the direction is towards that predicted in the simulations as seen in Fig. 12(a). If the droplet SMD becomes very small at the liquid length as suggested by the simulations, there would be an interesting decrease in PLV for droplets that are larger than $0.5 \mu\text{m}$ or increase in PLV in the Rayleigh regime if droplet size is smaller than $0.2 \mu\text{m}$. In other words, there is potential response to either increase or decrease the PLV at this region. However, the experimental extinction profile does not show signs of increased extinction, as related to a change in SMD in the Rayleigh regime rather than decreased liquid volume. Therefore, it is unlikely for droplets that are smaller than $0.5 \mu\text{m}$ to populate the regions upstream of the liquid length, the PLV slope would incline upward as opposed to continuously declining as predicted by the simulations. While uncertainties related to SMD must be considered, the most likely path is that of a decreasing PLV and droplet size. Such a path within SMD uncertainties is sketched on the figure, but it is obvious that detailed experiments on SMD and careful evaluation of simulations is needed in this region in the future. One item to be addressed in the next section is the persistence of smaller droplets if insufficient evaporation is predicted in the simulations.

4.2.2. Vapor–liquid equilibrium

To investigate the heat and mass transfer effect of the new modeling framework, this section presents a comparison between the current CFD approach and the assumption of adiabatic mixing and vapor–liquid equilibrium (VLE) vaporization. The equations for VLE applied to a 1D spray model with mixture of ambient gas and liquid are covered

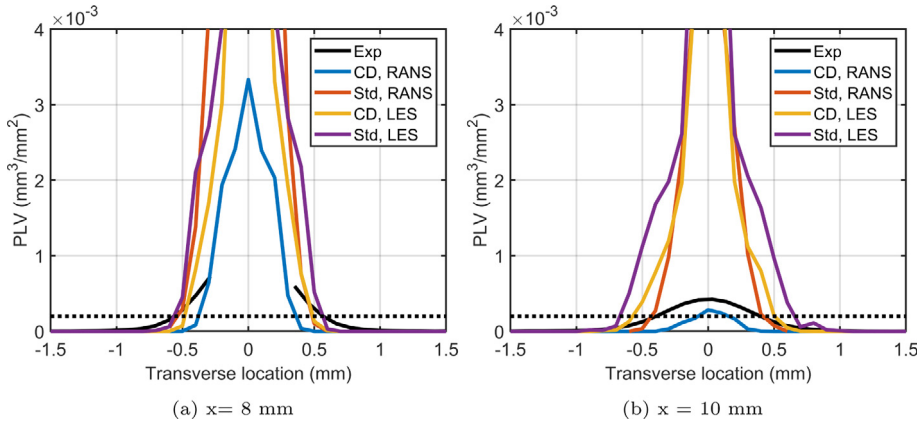


Fig. 11. Comparison of the transverse PLV profiles at different axial locations downstream of the injector.

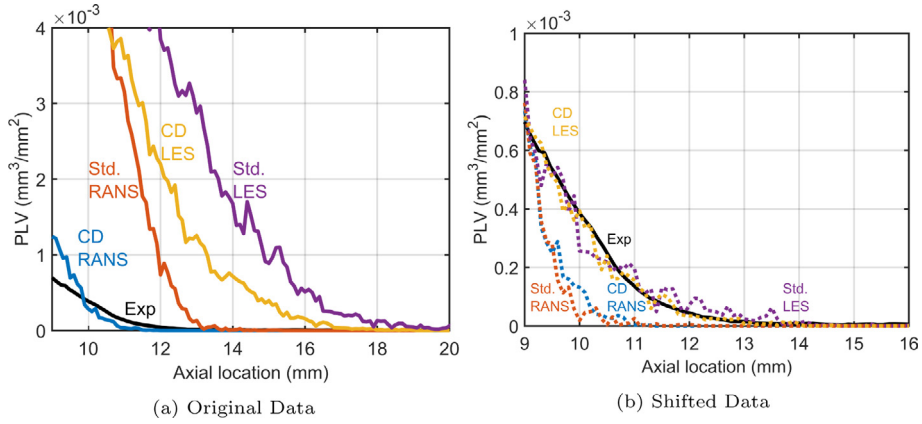


Fig. 12. Time-averaged projected liquid volume along the axis of the spray for different simulations.

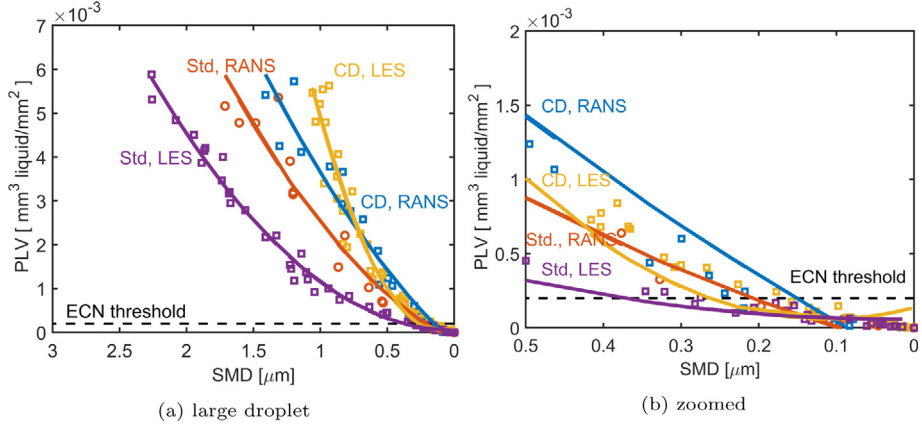


Fig. 13. Projected Liquid Volume as a function of droplet sizes in the near liquid length region.

by Desantes et al. (2007). The basic hypothesis is that if mixing drives vaporization, the liquid penetration will be the location where a saturated vapor condition exists and all liquid fuel is completely evaporated (Siebers, 1999), but there will also be substantial vaporization in VLE mixtures upstream of the liquid length. For the current Spray A condition, the saturated vapor mixture fraction value is 0.345. Because the model is constructed based on a steady-state assumption, the CFD results presented below are realization- and time-averaged with the same time-averaging period as the results shown in Figs. 12(a)–13.

In each Eulerian cell, we define the total mixture fraction as:

$$Y_f = \frac{m_{f,l} + m_{f,v}}{m_{f,l} + m_{f,v} + m_a}, \quad (35)$$

and the fuel vapor fraction as:

$$Y_{f,ratio} = \frac{m_{f,v}}{m_{f,l} + m_{f,v}}, \quad (36)$$

where $m_{f,l}$, $m_{f,v}$, m_a are the respective mass of the liquid fuel, vapor fuel, and ambient gas. Fig. 15(a) shows an example of the time-averaged

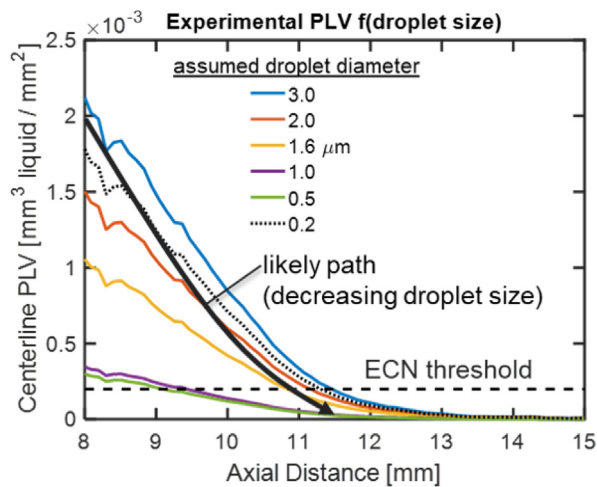


Fig. 14. Effect of different SMD assumptions on experimentally measured PLV axial profile.

axial slice of the total mixture fraction. Right outside of the nozzle, the total mixture fraction is close to one due to presence of liquid fuel. Fig. 15(b) shows a transverse mixture fraction profile comparison between the standard approach and CD model for the RANS simulation. For both simulations, there are leaner mixture found at the spray center compared to the spray edges, which is unphysical. Due to its enhanced evaporation characteristic, the CD model predicts richer mixture at the jet center compared to the standard approach, thus partially alleviating the issue. As we move further downstream, the CD model's enhanced evaporation gives better agreement with experimental data in PLV and liquid penetration predictions, as shown in Figs. 10–11.

To compare CFD to VLE mixtures, one approach is to plot the profile along the centerline of the spray, as illustrated by the broken horizontal line on Fig. 15(a). In this approach, the spray would naturally transition from a two-phase mixture to a pure vapor mixture as we move downstream from the nozzle exit and pass the liquid length, similar to the analysis performed by Desantes et al. (2007). Fig. 16 shows a comparison between the centerline CFD results and the VLE solution. The vertical dashed lines ($Y_f = 0.345$) mark the boundary between two different zones. The left zone denotes VLE mixtures with both liquid and vapor. The right zone marks the vapor-phase region, where at VLE, all of the liquid fuel has completely evaporated.

As shown in Fig. 16, the predicted mixture becomes saturated less than 2 mm downstream of the injector. If applied to a 1D model, it means the liquid penetrates up until only 2 mm. Obviously, this is a misleading observation created by nuances of the predicted mixture fraction distribution in the near-field of the injector. Fig. 15(b) shows total mixture fraction radial profile at 4 mm downstream from the injector for RANS simulations. At the center of the jet, the simulation predicts a saturated mixture value, and curiously, a richer mixture at the spray periphery. This behavior is rather unphysical, as experimental measurements show a richer mixture at the center of the jet (Pickett et al., 2014). The phenomenon, which causes more parcels to concentrate around the liquid spray periphery, demonstrates a current weaknesses of the current Lagrangian simulation approach. While the Corrected Distortion model somewhat alleviates this issue, as it predicts richer centerline mixture compared to the standard approach (Fig. 15(b)), more in-depth research addressing this problem should be conducted in the future.

To mitigate the false interpretation of an upstream saturated mixture (or even lower mixture fraction) far from the liquid length region, one can arbitrarily mark the upstream region (e.g: $x < 8$ mm) where the mixture fraction is below the theoretical saturated value by a different marker. Such an attempt is shown in Figs. 16(c)–16(d), where the

upstream region with mixture fraction less than the saturated mixture fraction is marked by the star symbol while the rest of the profiles are indicated by a circle symbol. For general clarity and purposes of interpretation of vaporization in the liquid length region, we focus on Figs. 16(e)–16(f), where the star symbols from Figs. 16(c)–16(d) are removed. Comparing Figs. 16(a) to 16(e) to 16(b) to 16(f), CFD results generally show higher vapor production than VLE in the region 2 mm from the injector, where the mixture fraction value is larger than 0.7. There is slightly incomplete vaporization ($Y_{f_{ratio}} < 1.0$) at mixture fractions value lower than saturated mixture fraction. Note that the CFD vaporization terms are not dictated by any direct relation to VLE, so it is easily possible to have vaporization that departs from the VLE curve. Note that the VLE formulations are developed for strictly adiabatic mixing and do not include any heat transfer effect caused by turbulence or stagnation phenomena.

A general observation is that the CD model generates more vaporization for a given mixture fraction compared to the standard model. While the shorter liquid penetration and smaller droplet size for the CD model have been demonstrated above, the comparison at the same mixture fraction affirms that the enhanced vaporization is a major characteristic of the model. Even with enhanced vaporization, however, the CD model does not predict complete vaporization at mean mixture fractions lower than saturated mixture fraction. One important distinction is that the symbols shown are for the mean mixture fraction, but the distribution shown in the shaded region fluctuates over a range of mixture fraction, and it may include instantaneous mixtures that are more fuel rich than the saturated mixture fraction, which can slow vaporization. The shaded region also suggests that it might be possible, at some random time instance, to have nearly complete vaporization even if the mixture value is slightly higher than theoretical saturated vapor value ($Z > 0.345$). This observation is a theoretical violation of VLE. A possible explanation is that the CFD is predicting higher mixture temperature compared to adiabatic mixing law, as the current heat/mass transfer model in either the Frossling vaporization (standard approach) and Corrected Distortion model does not explicitly enforce VLE behavior. Future research designed to address this question is currently planned.

4.3. Early spray behavior

The previous section qualitatively examines how the Corrected Distortion model affects spray behavior during the quasi-steady period. The CD model, however, also predicts significantly different spray behavior during the early stage of the injection process compared to the standard framework. The following section present a qualitative comparison of the spray characteristics during the early stage of the injection.

Fig. 17 shows transient comparison between the experimental PLV measurements and projected view of the Lagrangian parcels for all simulations during the early stage of injection. The droplets are painted by their temperature. For both RANS and LES using the standard approach, a mushroom-shaped droplet cloud forms around the liquid jet heads starting as early as 25 microseconds. This mushroom-shape cloud is populated by heated droplets, which have diminishing surface tension compared to colder upstream droplets, resulting in them being highly distorted. The Corrected Distortion framework, on the other hand, does not produce such behavior, which is consistent with experimental observations. Furthermore, the jet head in the Corrected Distortion model results are much hotter compared to the standard approach, thus illustrating the enhanced evaporation effect of the new model.

While the characteristic trend of having enhanced evaporation from the Corrected Distortion model are well captured in Fig. 17, the mushroom cloud is not as noticeable for LES compared to the RANS simulations. To provide further clarity on this behavior, two different sets of simulations were performed, one for RANS with a smaller cone angle of 15° and one for LES with a larger cone angle of 25° . In the RANS cases,

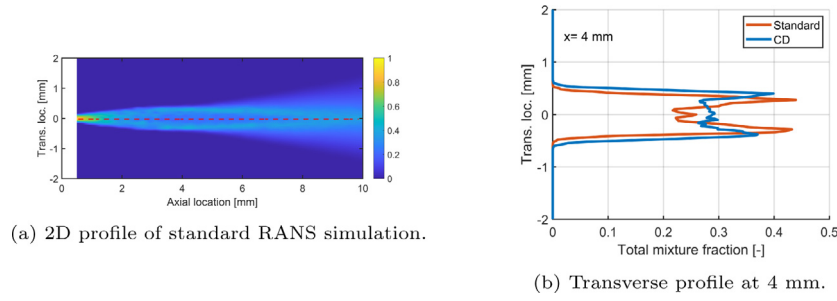


Fig. 15. Time-averaged total mixture fraction profiles for RANS simulations.

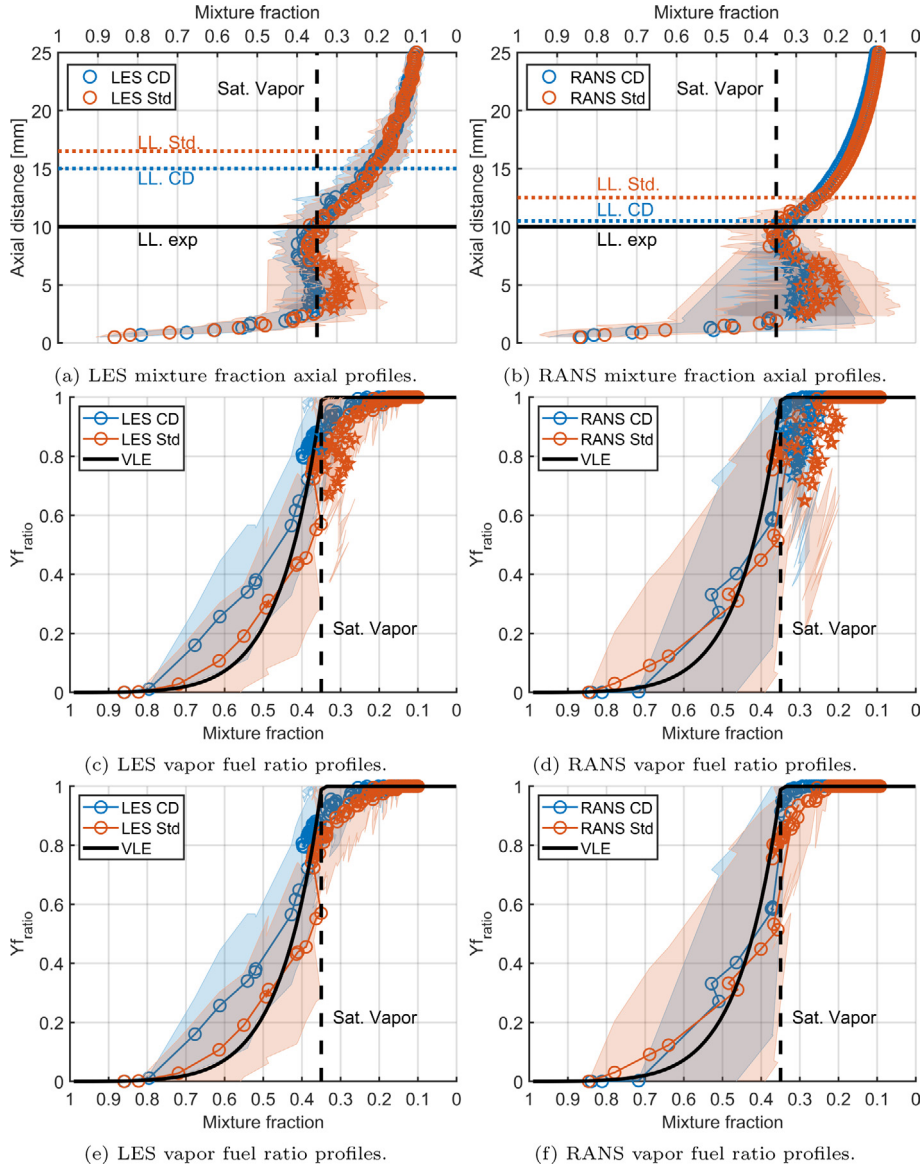


Fig. 16. Comparison of two-phase mixture fraction characteristics for all CFD simulations and vapor-liquid equilibrium theory.

the mushroom shape still appears for the standard approach despite using a smaller cone angle. For the LES cases, the mushroom shape becomes more visible for the standard models. Therefore, the Corrected Distortion model produces more realistic early spray behavior across different cone angle values. For brevity purposes, the results for these additional simulations are shown in Fig. 20 in Appendix.

Fig. 18 illustrates the CD model effect of enhanced evaporation for highly distorted oblate spheroid ($y > 0$) that is found surrounding the spray head in Fig. 17. In this figure, the y -axis is the drop mass transfer ratio, obtained by normalizing the Sherwood number calculated from the Corrected Distortion model (Eq. (25)) with the Sherwood number calculated by the Frossling correlation (Eq. (13)). One can conclude from Eq. (30) that a droplet with the maximum distortion factor

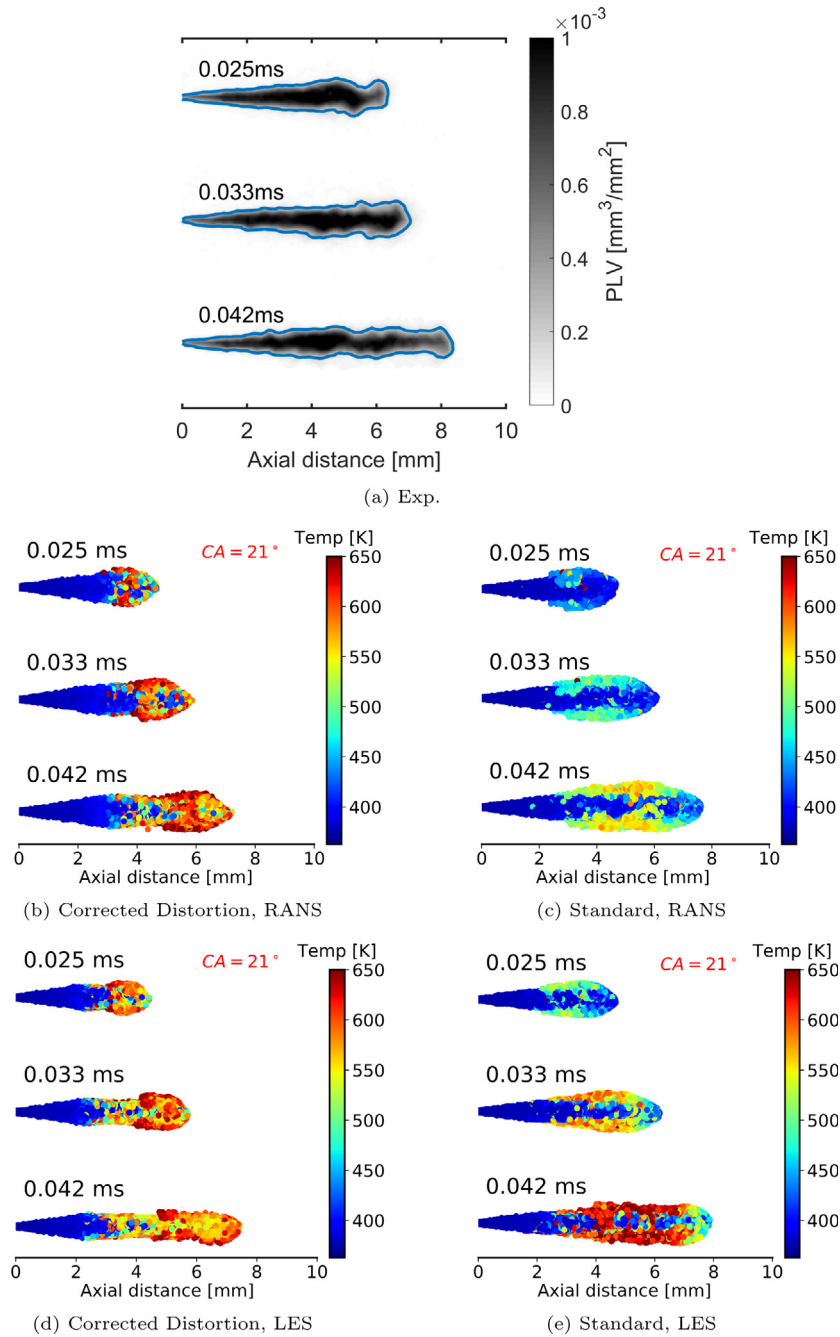


Fig. 17. Early transient spray behavior.

has only more than a 20% surface area compared to its spherical counterpart with the same equivalent radius. However, as indicated by Fig. 18, it has more than 3 times the evaporation rate compared to the equivalent undisturbed drop.

Fig. 19 shows the normalized drag coefficient comparison between the standard and Corrected Distortion models as a function of the distortion factor at an instance in time during the quasi-steady state ($t > 1$ ms). The coefficient is normalized by the baseline drag coefficient (Eq. (11)). For a highly distorted drop with the same distortion factor, the Corrected Distortion model predicts significantly lower drag compared to the standard approach. Furthermore, scattering of the data in the Corrected Distortion results illustrates finite viscosity effect, as opposed to the standard approach where the drag remains the same regardless of the drop's thermodynamic state.

4.4. Discussion on RANS vs. LES

Due to experimental capability at the time, previous works usually validate their simulation against experimental measurements in the vapor phase (Senecal et al., 2014; Kaario et al., 2020). However, the main shortcomings of vapor phase validation is that the measurements are only trustworthy much further downstream of the two-phase liquid region (e.g: 10 mm downstream of the liquid length). In this work, we can examine our liquid simulation results in details because of the new DBI experimental capability that is also augmented by our understanding of adiabatic mixing theory. Through such activity, it is very clear that there are substantial differences between RANS and LES. With the help of the CD model, RANS were able to agree with the PLV measurement in term of magnitude. However, as pointed

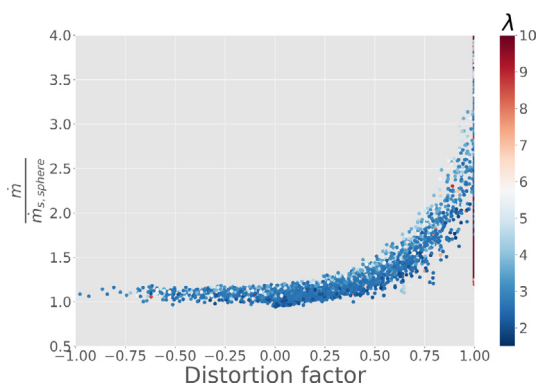


Fig. 18. Droplet mass transfer rate as a function of the distortion factor.

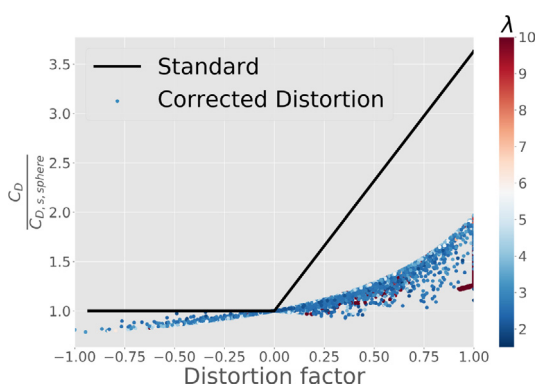


Fig. 19. Comparison between the drag coefficients. Results for the Corrected Distortion model are painted by the viscosity ratio (λ).

out by Figs. 11–12(a), the liquid jet in RANS decreases much faster in both axial and radial direction than observed in the experiment. From the same figures, regardless of the spray model, LES always overpredict PLV magnitude but produce more reasonable evaporation rate at the liquid length region. One possible explanation lies in the implementation and numerical setup. In this work, the minimum cell size in LES is half of its RANS counterpart. The spray coupling in CONVERGE uses nearest node kernel, where the exchanges between the two phases occur at the cell center regardless of the parcel position relative to the cell center. Results from such implementation are highly affected by mesh dependency issue, where the number of parcels per cell size is important (Schmidt and Bedford, 2018). From a formulation perspective, RANS is time-averaged, so its results are limited by the integral length scale of the problem and not the variation in cell size. While other researchers such as Garg et al. (2007) have demonstrated that introducing a polynomial interpolation scheme to the implementation reduces the mesh dependency issue, such approach will not likely result in a substantial change for RANS. However, interpolation to drop locations will be more significant for LES since the spatial filter size is the cell size itself. While a mesh dependency study has been carried out by Senecal et al. (2014), the lack of liquid phase comparison renders their results inconclusive in lieu of the new findings presented in this work. Future study, which is unfortunately outside of the scope of this work, should be carried out utilizing the same analysis presented here to provide additional insight.

5. Conclusions

The Corrected Distortion model, as presented in this work, provides a new framework toward more accurate mixture prediction that is crucial for Lagrangian engine spray simulations. By capturing more

realistic physics of highly distorted droplets, the new models predict enhanced evaporation while predicting lower drop drag compared to the standard approach. The new model results provide as good or better agreement with the experimental measurements of vapor mixture fraction, liquid velocities, liquid and vapor penetrations compared to the standard framework. The new modeling framework also results in better agreement with the One-D adiabatic mixing theory. While simulations of standard configuration such as Spray A do not hold any novelty, thorough analysis using the Projected Liquid Volume reveals an inconsistency. Specifically, the RANS simulations with the CD model agrees quite well with experimental data upstream but predict an over-mixed flow field downstream that diminishes the enhanced evaporation. In contrary, LES predicts better mixing field downstream, but with too much liquid upstream. While the CD model results are encouraging, especially with regards to drop drag and vaporization, there is definitely a need for an even better evaporation model. There is also a need to have a better understanding of the jet evolution in the near-field two-phase region with a transition to the far field. Variability in break up model constant, spray cone distribution, finite drop conductivity should be systematically examined. Applicability of the Corrected Distortion model for gasoline direct injection via ECN Spray G is currently under investigation.

CRedit authorship contribution statement

Tuan M. Nguyen: Software, Formal analysis, Validation, Visualization, Writing – original draft. **Rainer N. Dahms:** Conceptualization, Writing – review, Projection administration. **Lyle M. Pickett:** Experimental data analysis, Writing – review & editing, Project administration, Supervision. **Fabien Tagliante:** Data curation, Visualization, Writing – review & editing.

Declaration of competing interest

The authors declare that they have no known competing financial interests or personal relationships that could have appeared to influence the work reported in this paper.

Acknowledgments

This research was conducted as part of the Partnership for Advanced Combustion Engine (PACE) project sponsored by the Vehicle Technologies Office under the U.S. Department of Energy (DOE) Office of Energy Efficiency and Renewable Energy (EERE), with CPS Agreement 10033. The authors gratefully acknowledge Convergent Science Inc. for their licensing and technical supports. The authors also thank Dr. Shaoping Quan of Convergent Science for his support in implementing the original User Define Functions into CONVERGE 3.0 as a hidden feature.

Sandia National Laboratories is a multi-mission laboratory managed and operated by National Technology and Engineering Solutions of Sandia, LLC., a wholly owned subsidiary of Honeywell International, Inc., for the U.S. Department of Energy's National Nuclear Security Administration under contract DE-NA0003525. This paper describes objective technical results and analysis. Any subjective views or opinions that might be expressed in the paper do not necessarily represent the views of the U.S. Department of Energy or the United States Government

Appendix

A.1. Early PLV behavior

See Fig. 20.

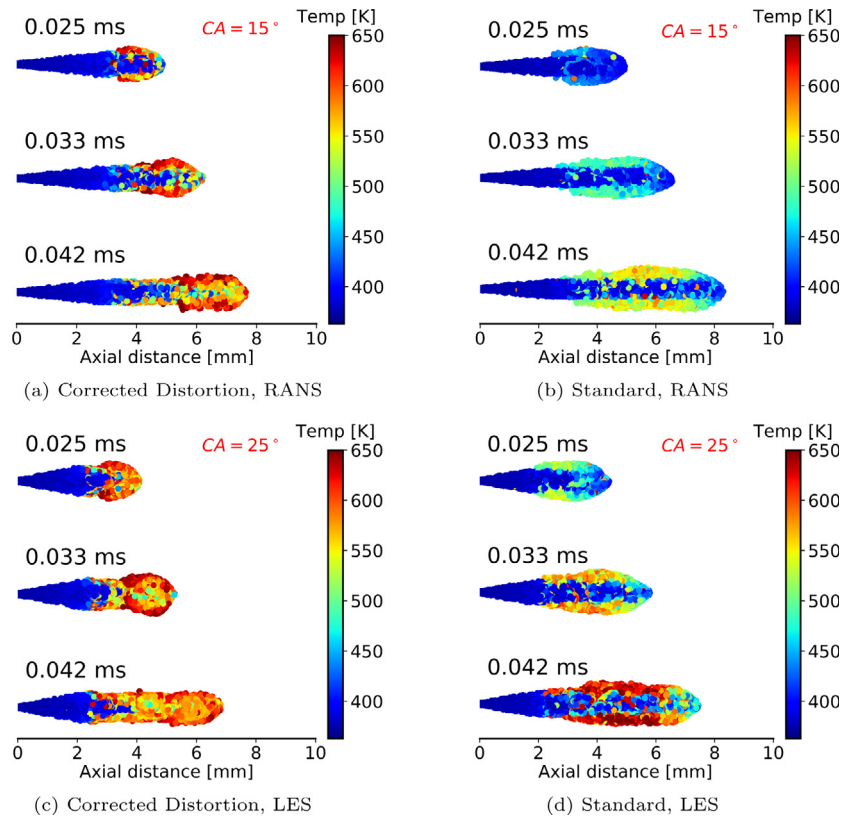


Fig. 20. Early transient spray behavior of RANS simulations with smaller cone angle ($CA = 15$) and LES with larger cone angle ($CA = 25$) compared to the main simulations.

References

- Abramzon, B., Sirignano, W.A., 1989. Droplet vaporization model for spray combustion calculations. *Int. J. Heat Mass Transfer* 32, 1605–1618. [http://dx.doi.org/10.1016/0017-9310\(89\)90043-4](http://dx.doi.org/10.1016/0017-9310(89)90043-4).
- Amsden, A., Butler, T., O'Rourke, P., 1987. The KIVA-II computer program for transient multidimensional chemically reactive flow with sprays. In: *SAE Technical Paper 872072*, vol. 96, pp. 373–383.
- Amsden, A., O'Rourke, P., Butler, T., 1989. Kiva-II: A computer program for chemically reactive flows with sprays, tech. rep., Los Alamos National Laboratory.
- Beale, J.C., Reitz, R.D., 1999. Modeling spray atomization with the kelvin-Helmholtz/Rayleigh-taylor hybrid model. *At. Spray*, 9, 623–650. <http://dx.doi.org/10.1615/AtomizSpr.v9.i6.40>.
- Crua, C., Manin, J., Pickett, L.M., 2017. On the transcritical mixing of fuels at diesel engine conditions. *Fuel* 208, 535–548. <http://dx.doi.org/10.1016/j.fuel.2017.06.091>.
- Dahms, R.N., Oefelein, J., 2016. The significance of drop non-sphericity in sprays. *Int. J. Multiph. Flow* 86, 67–85. <http://dx.doi.org/10.1016/j.ijmultiphaseflow.2016.07.010>.
- Desantes, J.M., Garcia-Oliver, J.M., Novella, R., Pachano, L., 2019. A numerical study of the effect of nozzle diameter on diesel combustion ignition and flame stabilization. *Int. J. Engine Res.* 21, 101–121. <http://dx.doi.org/10.1177/1468087419864203>.
- Desantes, J.M., Lopez, J., Garcia-Oliver, J.M., Pastor, J., 2007. Evaporative diesel spray modeling. *At. Spray*, 17, 193–231. <http://dx.doi.org/10.1615/AtomizSpr.v17.i3.10>.
- Engine Combustion Network, 2021. Engine Combustion Network, URL <https://ecn.sandia.gov/>.
- Engine Combustion Network, 2021. Spray A Recommended Rate of Injection, URL <https://ecn.sandia.gov/sprayaroi/>.
- Engine Combustion Network, 2021. Ambient Velocity, URL <https://ecn.sandia.gov/diesel-spray-combustion/sandia-cv/velocity-distribution/>.
- Engine Combustion Network, 2021. Liquid Penetration Length, URL <https://ecn.sandia.gov/diesel-spray-combustion/experimental-diagnostics/liquid-penetration-length/>.
- Faeth, G., 1977. Current status of droplet and liquid combustion. *Prog. Energy Combust. Sci.* 3, 191–224. [http://dx.doi.org/10.1016/0360-1285\(77\)90012-0](http://dx.doi.org/10.1016/0360-1285(77)90012-0).
- Feng, Z.-G., Michaelides, E., 2001a. Drag coefficients of viscous spheres at intermediate and high Reynolds numbers. *J. Fluids Eng.* 123, 841–849. <http://dx.doi.org/10.1115/1.1412458>.
- Feng, Z.-G., Michaelides, E., 2001b. Heat and mass transfer coefficients of viscous spheres. *Int. J. Heat Mass Transfer* 44, 4445–4454. [http://dx.doi.org/10.1016/S0017-9310\(01\)00090-4](http://dx.doi.org/10.1016/S0017-9310(01)00090-4).
- Garg, R., Narayanan, C., Lakehal, D., Subramaniam, S., 2007. Accurate numerical estimation of interphase momentum transfer in Lagrangian-Eulerian simulations of dispersed two-phase flows. *Int. J. Multiph. Flow* 33, 1337–1364. <http://dx.doi.org/10.1016/j.ijmultiphaseflow.2007.06.002>.
- Kaario, O.T., Vuorinen, V., Kahila, H., Im, H.G., Larmi, M., 2020. The effect of fuel on high velocity evaporating fuel sprays: Large-eddy simulation of spray a with various fuels. *Int. J. Engine Res.* 21, 26–42. <http://dx.doi.org/10.1177/1468087419854235>.
- Kastengren, A., Ilavsky, J., Viera, J.P., Payri, R., Duke, D., Swantek, A., Tilocco, F.Z., Sovis, N., Powell, C., 2017. Measurements of droplet size in shear-driven atomization using ultra-small angle x-ray scattering. *Int. J. Multiph. Flow* 92, 131–139. <http://dx.doi.org/10.1016/j.ijmultiphaseflow.2017.03.005>.
- Li, J., Zhang, J., 2014. A theoretical study of the spheroidal droplet evaporation in forced convection. *Phys. Lett. A* 378, 3537–3543. <http://dx.doi.org/10.1016/j.physleta.2014.10.020>.
- Liu, A., Mather, D., Reitz, R., 1993. Modeling the effects of drop drag and breakup on fuel sprays. In: *SAE Paper 930072*. <http://dx.doi.org/10.4271/930072>.
- Magnotti, G.M., Genzale, C., 2015. A NOVEL spray MODEL validation methodology USING LIQUID-phase extinction measurements. *At. Spray*, 25, 397–424. <http://dx.doi.org/10.1615/AtomizSpr.2014010377>.
- Malbec, L.-M., Bruneaux, G., Somers, B., Rousselle, C., Pickett, L.M., 2020. Identifying the driving processes of diesel spray injection through mixture fraction and velocity field measurements at ECN spray a. In: *SAE Technical Paper 2020-01-0831*. <http://dx.doi.org/10.4271/2020-01-0831>.
- Manin, J., Bardi, M., Pickett, L., 2012. Evaluation of the liquid length via diffused back-illumination imaging in vaporizing diesel sprays, in: *Proceedings of the 8th International Conference on Modeling and Diagnostics for Advanced Engine Systems, COMODIA 2012*, pp. 665–673.
- Meijer, M., Malbec, L.-M., Bruneaux, G., Somers, L., 2012. Engine combustion network: “spray a” basic measurements and advanced diagnostics. In: *12th Triennial International Conference on Liquid Atomization and Spray Systems. ICLASS, Heidelberg, Germany*.
- Musculus, M., Pickett, L.M., 2005. Diagnostic considerations for optical laser-extinction measurements of soot in high-pressure transient combustion environments. *Combust. Flame* 141, 371–391. <http://dx.doi.org/10.1016/j.combustflame.2005.01.013>.
- O'Rourke, P.J., Amsden, A.A., 1987. The tab method for numerical calculation of spray droplet breakup. In: *SAE Technical Paper 872089*. <http://dx.doi.org/10.4271/872089>.

- Paredi, D., Lucchini, T., D'Errico, G., Onorati, A., Pickett, L., Lacey, J., 2020. Validation of a comprehensive computational fluid dynamics methodology to predict the direct injection process of gasoline sprays using spray g experimental data. *Int. J. Engine Res.* 21, 199–216. <http://dx.doi.org/10.1177/1468087419868020>.
- Pickett, L.M., Genzale, C., Manin, J., 2015. Uncertainty quantification FOR LIQUID penetration OF evaporating sprays AT DIESEL-LIKE conditions. *At. Spray.* 25, 425–452. <http://dx.doi.org/10.1615/AtomizSpr.2015010618>.
- Pickett, L.M., Manin, J., Genzale, C.L., Siebers, D.L., Musculus, M.P., Idicheria, C.A., 2011. Relationship between diesel fuel spray vapor penetration/dispersion and local fuel mixture fraction. *SAE Int. J. Engines* 4, <http://dx.doi.org/10.4271/2011-01-0686>.
- Pickett, L., Manin, J., Kastengren, A., Powell, C., 2014. Comparison of near-field structure and growth of a diesel spray using light-based optical microscopy and X-Ray radiograph. *SAE Int. J. Engines* 7, 1044–1053. <http://dx.doi.org/10.4271/2014-01-1412>.
- Ranz, W.E., Marshall, W., 1952. Evaporation from drops. *Chem. Eng. Prog.* 48, 141–173.
- Richards, K.J., Senecal, P.K., Pomraning, E., 2020a. CONVERGE 3.0 Manual. Convergent Science.
- Richards, K.J., Senecal, P.K., Pomraning, E., 2020b. CONVERGE 3.0. Convergent Science.
- Richter, A., Nikrityuk, P.A., 2012. Drag forces and heat transfer coefficients for spherical, cuboidal and ellipsoidal particles in cross flow at sub-critical Reynolds numbers. *Int. J. Heat Mass Transfer* 55, 1343–1354. <http://dx.doi.org/10.1016/j.ijheatmasstransfer.2011.09.005>.
- Schmidt, D.P., Bedford, F., 2018. An analysis of the convergence of stochastic Lagrangian/Eulerian spray simulations. *Int. J. Multiph. Flow.* 102, 95–101. <http://dx.doi.org/10.1016/j.ijmultiphaseflow.2018.01.024>.
- Schmidt, D.P., Rutland, C.J., 2000. A new droplet collision algorithm. *J. Comput. Phys.* 164, <http://dx.doi.org/10.1006/jcph.2000.6568>.
- Senecal, P.K., Pomraning, E., Richards, K.J., Som, S., 2012. Grid-convergent spray models for internal combustion engine cfd simulations. In: Vol. ASME 2012 Internal Combustion Engine Division Fall Technical Conference of Internal Combustion Engine Division Fall Technical Conference. pp. 697–710. <http://dx.doi.org/10.1115/ICEF2012-92043>.
- Senecal, P., Pomraning, E., Xue, Q., Som, S., Banerjee, S., Hu, B., Liu, K., Deur, J., 2014. Large eddy simulation of vaporizing sprays considering multi-injection averaging and grid-convergent mesh resolution. *J. Eng. Gas Turbines Power* 136 (11), <http://dx.doi.org/10.1115/1.4027449>.
- Senecal, P., Richards, K., Pomraning, E., Yang, T., Dai, M.Z., McDavid, R.M., Patterson, M.A., Hou, S., Shethaji, T., 2007. A new parallel cut-cell cartesian CFD code for rapid grid generation applied to in-cylinder diesel engine simulations. In: SAE Technical Paper. <http://dx.doi.org/10.4271/2007-01-0159>.
- Siebers, D.L., 1998. Liquid-phase fuel penetration in diesel. *SAE Trans.* 107, 1205–1227.
- Siebers, D.L., 1999. Scaling liquid-phase fuel penetration in diesel sprays based on mixing-limited vaporization. In: SAE Technical Paper 1999-01-0528. SAE International, <http://dx.doi.org/10.4271/1999-01-0528>.
- Sirignano, W.A., 1983. Fuel droplet vaporization and spray combustion theory. *Prog. Energy Combust. Sci.* 9, 291–322. [http://dx.doi.org/10.1016/0360-1285\(83\)90011-4](http://dx.doi.org/10.1016/0360-1285(83)90011-4).
- Som, S., D'Errico, G., Longman, D., Lucchini, T., 2012. Comparison and standardization of numerical approaches for the prediction of non-reacting and reacting diesel sprays. In: SAE Technical Paper 2012-01-1263. <http://dx.doi.org/10.4271/2012-01-1263>.
- Sommerfeld, M., Ando, A., Wennerberg, D., 1992. Swirling, particle-laden flows through a pipe expansion. *J. Fluids Eng.* 114, 648–656. <http://dx.doi.org/10.1115/1.2910081>.
- Sphicas, P., Pickett, L.M., Skeen, S., Frank, J., Lucchini, T., Sinoir, D., D'Errico, G., Saha, K., Som, S., 2017. A comparison of experimental and modeled velocity in gasoline direct-injection sprays with plume interaction and collapse. *SAE Int. J. Fuels Lubr.* 10, 184–201. <http://dx.doi.org/10.4271/2017-01-0837>.
- Stetsyuk, V., Turner, J., Crua, C., Pearson, R., Gold, M., 2015. Droplet size and morphology characterization for diesel sprays under atmospheric operating conditions. In: 13th Triennial International Conference on Liquid Atomization and Spray Systems. ILASS Americas, Tainan, Taiwan.
- Tonini, S., Cossali, G., 2013. An exact solution of the mass transport equations for spheroidal evaporating drops. *Int. J. Heat Mass Transfer* 60, 236–240. <http://dx.doi.org/10.1016/j.ijheatmasstransfer.2013.01.001>.
- Tonini, S., Cossali, G., 2014. An evaporation model for oscillating spheroidal drops. *Int. Commun. Heat Mass Transfer* 51, 18–24. <http://dx.doi.org/10.1016/j.icheatmasstransfer.2013.12.001>.
- Tryggvason, G., Scardovelli, R., Zaleski, S. (Eds.), 2011. *Direct Numerical Simulations of Gas-Liquid Multiphase Flows*. Cambridge University Press.
- Westlye, F.R., Penney, K., Ivarsson, A., Pickett, L.M., Manin, J., Skeen, S.A., 2017. Diffuse back-illumination setup for high temporally resolved extinction imaging. *Appl. Opt.* 56, 5028–5038. <http://dx.doi.org/10.1364/AO.56.005028>.
- Zhang, L., Tadashi, T., Ueda, T., Itou, Y., Tomoyuki, I., Yokota, K., 1997. Measurements of liquid phase penetration of evaporating spray in a di diesel engine. In: SAE Paper No. 971645. <http://dx.doi.org/10.4271/971645>.
- Zubkov, V., Cossali, G., Tonini, S., Rybdylova, O., Crua, C., Heikal, M., Sazhin, S., 2017. Mathematical modelling of heating and evaporation of a spheroidal droplet. *Int. J. Heat Mass Transfer* 108, 2181–2190. <http://dx.doi.org/10.1016/j.ijheatmasstransfer.2016.12.074>.